Curvilinear Structure Tracking Based on Dynamic Curvature-penalized Geodesics

Li Liu, Mingzhu Wang, Shuwang Zhou, Minglei Shu, Laurent D. Cohen, Da Chen

▶ **To cite this version:**

Li Liu, Mingzhu Wang, Shuwang Zhou, Minglei Shu, Laurent D. Cohen, et al.. Curvilinear Structure Tracking Based on Dynamic Curvature-penalized Geodesics. Pattern Recognition, 2023, 134, pp.109079. 10.1016/j.patcog.2022.109079 . hal-03863441

HAL Id: hal-03863441
https://hal.science/hal-03863441

Submitted on 21 Nov 2022

HAL is a multi-disciplinary open access archive for the deposit and dissemination of scientific research documents, whether they are published or not. The documents may come from teaching and research institutions in France or abroad, or from public or private research centers.

L'archive ouverte pluridisciplinaire **HAL**, est destinée au dépôt et à la diffusion de documents scientifiques de niveau recherche, publiés ou non, émanant des établissements d'enseignement et de recherche français ou étrangers, des laboratoires publics ou privés.

Revised Manuscript (Clean version)

Curvilinear Structure Tracking Based on Dynamic Curvature-penalized Geodesics

Li Liu[a], Mingzhu Wang[b], Shuwang Zhou[a], Minglei Shu[a,*], Laurent D. Cohen[c], Da Chen[a]

[a] *Shandong Artificial Intelligence Institute, Qilu University of Technology (Shandong Academy of Sciences), Jinan, China*
[b] *Yueyang Hospital of Integrated Traditional Chinese and Western Medicine, Shanghai University of Traditional Chinese Medicine, Shanghai, China*
[c] *Université Paris Dauphine, PSL Research University, CNRS, UMR 7534, CEREMADE, 75016 Paris, France*

Abstract

Geodesic models are considered as a fundamental and powerful tool in the applications of curvilinear structure extraction, where the target structures are usually modeled as geodesic paths connecting prescribed points. Despite great advances in geodesic models, it still remains an unsolved problem of detecting weak curvilinear structures from complicated scenarios. In this paper, a dynamic high-order geodesic model for curvilinear structure extraction is introduced to alleviate the shortcuts or short branches combination problems suffered in the classical geodesic approaches. For that purpose, we take into account the nonlocal pattern of curvilinear structures and the local curvature of geodesic paths for the construction of geodesic metrics. Accordingly, the proposed model is able to blend the benefits from the on-the-fly nonlocal smoothness property, curvature regularization and appearance coherence penalization. The nonlocal smoothness property carried out via a local bending operator is constructed to provide a quantitative measure of geodesic advancing directions, meanwhile the coherence penalization is established to guarantee the consistency of the local appearance features extracted via a vessel detector. The experiment results on synthetic and real images illustrate that the proposed method obtains outper-

*Corresponding author

formance when compared to the classical geodesic-based tracing algorithms.

Keywords: Curvature-penalized geodesics, local bending constraint, coherence penalization, curvilinear structures, retinal vessels

1. Introduction

The curvilinear structure tracking is a crucial problem in the field of computer vision and image analysis. There are many important applications such as the quantitative analysis of vessel structures in medical images for disease diagnosis and surgical navigation, the detection of roads and rivers in satellite images for measurement and planning.

The curvilinear structure tracking is a challenging task due to the high variability shape and complicated background. Various methods have been developed to solve the problem including the graph-based models [1, 2], the curve evolution-based methods [3, 4], the learning-based approaches [5, 6], the low rank-based algorithms [7, 8] and the geodesic path-based models [9, 10, 11]. More details about the main features of the models can be found in Table 1. Among them, the learning-based approaches have achieved impressive performance in general segmentation problems by utilizing a set of annotated data for training [12, 13, 14]. However, this kind of method can not make sure that the detected result is continuous especially when the curvilinear structure has weak appearance features. The geodesic model as an effective tracing tool provides a more elegant solution for continuous curvilinear structure tracking benefitting from its global optimization performance and fast numerical solvers. It regards the centerline of the target structure as the geodesic between source and end points. The geodesic path can be tracked on the geodesic distance map obtained by propagating a wavefront from the source point based on geodesic metrics [15].

The manuscript is organized as follows. In Section 2, we briefly introduce the related works. Section 3 desribes the background on the Euler-Mumford elastica geodesic model. Section 4 presents the core contribution of this manuscript. In Sections 5 and 6, we present the experimental results and the conclusion.

2. Related work

We give a short review of the previous geodesic path-based models in two related areas including automatic and interactive geodesic-based methods.

2.1. Automatic Geodesic-based Methods

Different kinds of automatic geodesic-based methods have been studied with aim to extract all the branches of the curvilinear tree structure. The minimal path growing methods trace the connected tree structure by regarding source points as a series of key points detected automatically during the course of the geodesic distance calculation until the stop criteria are met [11, 9], however it is hard to design effectively propagation stopping strategy especially for complex scenario. The geodesic voting methods try to track the complete curvilinear structure by finding image points with high geodesic density [16]. The target structures with low appearance features usually have low density values. Then the backtracking strategy is introduced in the minimal path propagation in order to detect all branches of the tree structure [17]The minimum spanning trees model detects the structure by finding saddle points from the geodesic distance map [18].However, those methods lack reliability in complex scenario, especially failing to detect fragile structures with disconnections or misconnections.

2.2. Interactive Geodesic-based Methods

For the interactive geodesic approaches, various geodesic metrics have been studied for curvilinear structure tracking in different situations. The original geodesic model [15] is built upon the type of isotropic Riemannian metrics which are position-dependent only. Then it is extended to a more general anisotropic case [19, 20] depending both on path position and orientation information, which is conducted by taking into account the tubular anisotropy features [21, 22].

Furthermore, geodesic metrics considering radii or orientations are proposed by adding abstract dimensions to the image domain, so a planar curve can be

described by a high-dimensional geodesic path. A basic objective of the radius-lifted geodesic models is to search for the centerline and boundaries of the curvilinear structure simultaneously. The geodesic model with isotropic radius-lifted Riemannian metric [10] compute the geodesic path containing the physical position and radius values. Then, the anisotropic cases [23] are introduced by lifting the anisotropic metric [19, 20] to the radius-lifted space. Geodesic models in orientation-lifted space provide a novel way to utilize the orientation information. The isotropic orientation-lifted Riemannian metric is proposed to search the geodesic path in the orientation-lifted domain [24]. Moreover, a Riemannian metric [25] is designed by adding orientation dimension to the radius-lifted domain simultaneously. More importantly, the curvature information [26, 27] can be introduced into the geodesic model depending on the orientation-lifted scheme. The geodesic paths with rigid enhancement associated to Finsler elastica metric [28] or sub-Riemannian metric [29] can be calculated by utilizing the curvature-penalized fast marching approach [30]. The introduction of curvature penalization makes a significant breakthrough in geodesic model, which effectively improve its ability to detect curvilinear structures with complex topologies and scenes.

The geodesic models mentioned above are limited to the scope such that their metrics are fixed during the geodesic distance computation. This means that the metrics in these models cannot benefit from the nonlocal geometric features generated during the fast marching front propagation. In order to remove this limitation, the approaches using dynamic metrics are proposed in [31, 32, 33, 34, 35, 36]. Specifically, Liao et al. [31, 36] introduced an effective dynamic geodesic model by incorporating nonlocal path-based features to steer the front propagation progressively. In this model, the metric used is limited in the isotropic case. Such an idea is then adapted by [32] to the anisotropic tubular model established in the radius-lifted space, thus able to simultaneously delineate the centerline and boundaries of the curvilinear structures. Finally, the nonlocal tubular appearance coherence penalty is introduced into the dynamic anisotropic Riemannian metric, which is helpful to detect tar-

Table 1: Illustration the main features of the related works.

Models	**Advantages**	**Disadvantages**
Graph-based models	Global optimum	Difficult to remove background structures
Curve evolution-based models	Automatic detection	Stuck in undesirable local minima
Learning-based models	Multi-target tracking	Manual annotation
Low rank-based models	Multi-target tracking	Noise sensitive
Automatic geodesic-based models	All branches detection	Lack reliability in complex scenario
Interactive geodesic-based models	Global optimum	Shortcuts/short branches combination problems

get structures with weak appearance features [33]. In summary, the existing geodesic models featuring dynamic metrics can reduce the risk of shortcuts and short branches combination problems in some extent. However, these dynamic models do not consider the curvature penalization which is an important regularization term in curvilinear structure tracking, thus limiting their practical applications.

2.3. Our Contribution

In this work, we introduce a new method for constructing dynamic metrics which embedd curvature penalization, in order to overcome the shortcuts and short branch combination problems occurring when tracing curvilinear structures featuring complex geometry, long euclidean curve length or strong tortuosity. The key ingredients of the proposed model involve: i) estimating the bending measures of locally back-tracked paths to control the advancing directions of the fast marching fronts, and ii) incorporating the coherence penalization of curvilinear appearance features into the construction of dynamic metrics.

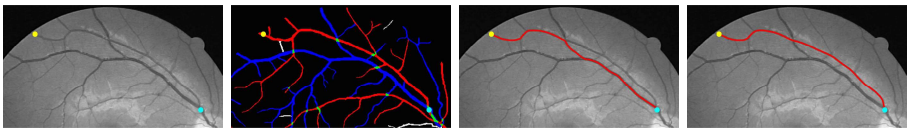

(a) (b) (c) (d)

Figure 1: An example for illustrating the short branches combination problem. (**a**) and (**b**) Image patch and ground truth with source (cyan) point and end (yellow) point. The objective is to extract the artery vessel (red) between two given points. (**c**) Vessel extraction results via the Finsler Elastica minimal path model [28] and the short branches combination problem occurs. (**d**) The geodesic path derived from the proposed model indeed seeks the correct vessel

Basically, the proposed method differs to the existing dynamic geodesic models in the consideration of curvature penalization that is an important geometric property in curvilinear structure extraction. In addition, comparing to the traditional curvature-penalized models [28, 30, 29], our model leverages additional nonlocal path-based features and appearance coherence to generate more accurate results, as illustrated in Fig. 1. The short branches combination problem occurs when the target geodesic path passes through some segments belonging to different vessels. In Figs. 1a and 1b, the original retinal vessel image and the corresponding groundtruth of artery (red regions) and vein (blue regions) vessels are illustrated, respectively. The goal is to extract the artery vessel between the given points. We can see that the geodesic paths from elastica model [28] suffer from the short branches combination problems as shown in Fig. 1c, while the proposed model can accurately find the target.

3. Background on Curvature-penalized Geodesic Model

3.1. Multi-orientation Geometry Description

Let $\Omega \subset \mathbb{R}^2$ denote an open and bounded image domain, and let $\hat{\Omega} := \Omega \times \mathbb{R}_{\text{scale}} \subset \mathbb{R}^3$ represent radius-lifted domain, where $\mathbb{R}_{\text{scale}} = [\mathcal{R}_{\min}, \mathcal{R}_{\max}]$ indicates the radius space. For a point $\hat{x} \in \hat{\Omega}$, it is a pair (x, r) where $x \in \Omega$ and $r \in \mathbb{R}_{\text{scale}}$. In the application of curvilinear structure tracking, it is important to detect the orientations and positions of the targets. In this work, the optimally

Table 2: Annotation for the key math notations used in this work.

Notation	Annotation	Notation	Annotation
Ω	Image domain	$\mathbb{M}$	Orientation-lifted space
$\mathbb{R}_{\text{scale}}$	Radius space	$\mathbb{S}^1$	Orientation space
Ψ	OOF filte responser	$\mathbf{H}$	Hessian matrix
Υ	Indicator of a disk	ρ	Optimal scale map
η	Unit vector	ψ_{score}	Vessel score map
ψ_{os}	Orientation score map	κ	Curvature of the curve
γ	Lipschitz curve	$\tilde{\gamma}$	Orientation-lifted curve
$\mathcal{D}$	Geodesic distance map	$\mathcal{C}$	Geodesic path
Φ	Appearance features	Θ	Main orientation set
$\mathfrak{p}$	Potential function	ρ	Optimal scale map
ϕ	Coherence penalty	ς	Optimal orientation
χ	Local bending measure	$\mathfrak{g}$	Local bending constraint

oriented flux (OOF) filter is used to extract the appearance features and orientation information, which is adopted to estimate the presence of curvilinear structure from the background [37]. Without loss of generality, the gray levels of the curvilinear structures are assumed to appear to be locally lower than background.

The response Ψ of the OOF filter at a position $x \in \Omega$ with a radius r is encoded in a symmetric matrix of size 2×2 as

$$\Psi(x, r) = \frac{1}{r}\big(\mathbf{H}(G_\sigma) * \Upsilon_r * I\big)(x), \tag{1}$$

where $I : \Omega \to \mathbb{R}$ is a gray level image, $\mathbf{H}(G_\sigma)$ is the Hessian matrix of a Gaussian kernel G_σ with standard deviation σ, and Υ_r is the indicator of a disk with radius r. For the 2D curvilinear structure tracking problem, the response Ψ can be expressed by its eigenvalues with assumption $\lambda_i(\cdot)$ $(i = 1, 2)$ and the corresponding eigenvectors $\mathbf{v}_i(\cdot)$. Without loss of generality, the eigenvalues are assumed $0 \approx \lambda_1(\cdot) \leq \lambda_2(\cdot)$. These eigenvalues characterizing the appearance

features can be applied to estimate the optimal radius of a point at the centerline of a curvilinear structure, by defining an optimal scale map $\rho : \Omega \to \mathbb{R}_{\text{scale}}$ from $\lambda_2(x, r)$ as

$$\rho(x) = \underset{r \in \mathbb{R}_{\text{scale}}}{\arg\max} \{\lambda_2(x, r)\}. \tag{2}$$

A vessel score map ψ_{score}, indicating the likelihood of a point x belongs to a curvilinear structure centerline, can be derived at optimal scale as

$$\psi_{\text{score}}(x) = \max \{\lambda_2(x, \rho(x)), 0\}. \tag{3}$$

For a point x inside the curvilinear structures, the eigenvector $\mathbf{v}_1(x, \rho(x))$ provides the curvilinear structure direction for the point x lying inside it.

Let $\mathbb{S}^1 = [0, 2\pi)$ represent the orientation space with a periodic boundary condition, and let $\mathbb{M} := \Omega \times \mathbb{S}^1$ denote the orientation-lifted space. A point $\mathbf{x} = (x, \theta) \in \mathbb{M}$ is made up of a physical position $x \in \Omega$ and an angular component $\theta \in \mathbb{S}^1$. Let $\eta_\theta = (\cos\theta, \sin\theta)^T$ denote a unit vector of the orientation $\theta \in \mathbb{S}^1$. The orientation-dependent scores $\psi_{\text{os}} : \mathbb{M} \to \mathbb{R}^+$ can be defined

$$\psi_{\text{os}}(x, \theta) = \max\{\langle \eta_\theta^\perp, \Psi(x, \rho(x))\eta_\theta^\perp \rangle, 0\}, \tag{4}$$

where $\eta_\theta^\perp$ is perpendicular to the unit vector η_θ. The orientation scores have the ability to extend the confidence map Ψ to a orientation-lfited space [28].

3.2. Euler-Mumford Elastica Geodesic Model

The curvature-penalized geodesic models exploit the curvature as the regularization for computing smooth geodesic curves. Significant examples of existing curvature-penalized geodesic approaches involve the Euler-Mumford elastica model [28], the Reeds-Sheeps models [29] and the Dubins car model [30]. In this work, we take the Euler-Mumford elastica model as the basis of the proposed geodesic model. In the remaining of this section, we briefly introduce the elastica model involving the orientation-lifted geodesic metric and the associated eikonal equation.

Let $\text{Lip}([0, 1], \Omega)$ represent the set of Lipschitz continuous curves $\gamma : [0, 1] \to \Omega$. The Euler-Mumford elastica model [28] utilizs a squared curvature term to

establish the weighted curve length of a smooth curve $\gamma : [0,1] \to \Omega$ as

$$\mathcal{L}(\gamma) := \int_0^1 \zeta(\gamma(u), \gamma'(u))(1 + \beta^2 \kappa(u)^2) \|\gamma'(u)\| du, \tag{5}$$

where $\zeta : \Omega \times \mathbb{R}^2 \to \mathbb{R}^+$ is a data-driven cost function derived from the image features, $\kappa : [0,1] \to \mathbb{R}$ denotes the curvature of the smooth curve $\gamma : [0,1] \to \Omega$ and γ' is its first-order derivative. The parameter $\beta > 0$ is a constant controlling the importance of the curvature. In order to minimize the length (5) featuring second-order property of curves, an orientation-lifting strategy is exploited, in conjunction with a parametric function $\vartheta : [0,1] \to \mathbb{S}^1$ which represents the turning angle of a smooth curve γ as

$$\gamma'(u) = \eta_\vartheta \, \|\gamma'(u)\|, \tag{6}$$

yielding that for any $u \in [0,1]$

$$\kappa(u) = \frac{\vartheta'(u)}{\|\gamma'(u)\|}. \tag{7}$$

In this case, the curve γ is mapped to an orientation-lifted curve $\tilde{\gamma}(u) = (\gamma(u), \vartheta(u)) \in \mathbb{M}$. Incorporating the representation (7) to the length (5), the energy functional is obtained as following

$$\mathfrak{L}(\tilde{\gamma}) = \int_0^1 \zeta(\gamma(u), \vartheta(u)) \left(\|\gamma'(u)\| + \frac{|\beta \vartheta'|^2}{\|\gamma'(u)\|} \right) du, \tag{8}$$

subject to the assumption (6).

The length (8) related to the elastica geodesic metric [28] $\mathcal{F} : \mathbb{M} \times \mathbb{R}^3 \to \mathbb{R}_0^+$ reads for any point $\mathbf{x} = (x, \theta) \in \mathbb{M}$ and any vector $\dot{\mathbf{x}} = (\dot{x}, \dot{\theta}) \in \mathbb{R}^3$ as follows

$$\mathcal{F}(\mathbf{x}, \dot{\mathbf{x}}) = \begin{cases} \|\dot{x}\| + \frac{|\beta \dot{\theta}|^2}{\|\dot{x}\|}, & \text{if } \dot{x} = \eta_\theta \|\dot{x}\|, \\ \infty, & \text{otherwise.} \end{cases} \tag{9}$$

yielding an equivalent expression of $\mathfrak{L}$ as

$$\mathfrak{L}(\tilde{\gamma}) = \int_0^1 \zeta(\gamma, \vartheta) \mathcal{F}(\tilde{\gamma}, \tilde{\gamma}') du, \tag{10}$$

where the image data-driven function $\zeta : \Omega \times \mathbb{R}^2 \to \mathbb{R}^+$ can be constructed based on the orientation-dependent scores ψ_{os} defined in Eq. (4) with a weighted

parameter $\alpha \in \mathbb{R}^+$ as

$$\zeta(\mathbf{x}) = \exp(-\alpha\, \psi_{\text{os}}(\mathbf{x})). \tag{11}$$

Therefore, the minimization of the energy in Eq. (5) can be approximately addressed by seeking the minimal path of the weighted curve length $\mathfrak{L}$, which can be solved by the Eikonal PDE framework.

Given a source point $\mathbf{s} \in \mathbb{M}$ and a target point $\mathbf{x} \in \mathbb{M}$, the geodesic path $\mathcal{C}_{\mathbf{s},\mathbf{x}} : [0,1] \to \mathbb{M}$ linking from $\mathbf{s}$ to $\mathbf{x}$ globally minimizes the length (10) among the set $\text{Lip}([0,1],\mathbb{M})$ of all Lipchitz continuous curves $\tilde{\gamma} : [0,1] \to \mathbb{M}$

$$\mathcal{C}_{\mathbf{s},\mathbf{x}} = \underset{\tilde{\gamma}\in \text{Lip}([0,1],\mathbb{M})}{\arg\min} \{\mathfrak{L}(\tilde{\gamma}); \tilde{\gamma}(0) = \mathbf{s}, \tilde{\gamma}(1) = \mathbf{x}\}. \tag{12}$$

The geodesic path $\mathcal{C}_{\mathbf{s},\mathbf{x}}$ contains the spatial positions of a tubular centerline. The geodesic distance map $\mathcal{D}_{\mathbf{s}}$ defined as the length of $\mathcal{C}_{\mathbf{s},\mathbf{x}}$, i.e.

$$\mathcal{D}_{\mathbf{s}}(\mathbf{x}) = \min_{\tilde{\gamma}\in \text{Lip}([0,1],\mathbb{M})} \left\{\mathfrak{L}(\tilde{\gamma})\right\},\ s.t.\ \begin{cases} \tilde{\gamma}(0) = \mathbf{s} \\ \tilde{\gamma}(1) = \mathbf{x}. \end{cases} \tag{13}$$

The geodesic distance map $\mathcal{D}_{\mathbf{s}}$ admits the unique viscosity solution to a generalized Eikonal equation

$$\mathcal{H}_{\mathbf{x}}(\nabla \mathcal{D}_{\mathbf{s}}(\mathbf{x})) = \frac{1}{2}\zeta(\mathbf{x})^2, \forall \mathbf{x} \in \mathbb{M}\backslash\{\mathbf{s}\} \tag{14}$$

with a boundary condition $\mathcal{D}_{\mathbf{s}}(\mathbf{s}) = 0$, where $\mathcal{H}$ is the elastica Hamiltonian [30] defined as the Legendre-Fenchel conjugate of $(\frac{1}{2}\mathcal{F})^2$

$$\mathcal{H}_{\mathbf{x}}(\hat{\mathbf{x}}) = \frac{1}{8}\left(\langle \hat{\mathbf{x}}, \eta_\theta\rangle + \sqrt{\langle \hat{\mathbf{x}}, \eta_\theta\rangle^2 + (\hat{\theta}/\beta)^2}\right)^2. \tag{15}$$

for any point $\mathbf{x} \in \mathbb{M}$ and any co-vector $\hat{\mathbf{x}} = (\hat{x}, \hat{\theta}) \in \mathbb{R}^3$.

The target geodesic path $\mathcal{C}_{\mathbf{s},\mathbf{x}}$ can be obtained by re-parameterizing a geodesic curve $\mathcal{C}_*$ which is the solution to the following ODE

$$\mathcal{C}'_*(u) = \mathbf{V}(\mathcal{C}_*(u)), \quad \text{with } \mathcal{C}_*(0) = \mathbf{x}, \tag{16}$$

where $\mathbf{V}$ is the geodesic flow defined as

$$\mathbf{V}(\mathbf{x}) := \underset{\|\hat{\mathbf{v}}\|=1}{\arg\max} \frac{\langle \hat{\mathbf{v}}, \dot{\mathbf{x}}\rangle}{\mathcal{F}(\mathbf{x}, \dot{\mathbf{x}})}. \tag{17}$$

The ODE (16) is solved backward in time till the source point $\mathbf{s}$ is reached. Numerically, it can be solved via a finite differences scheme [30].

3.3. Motivation

In the practical applications of curvilinear structure tracking, one of the basic objects is to delineate the target structure between two given points. The classic geodesic models treat the centerline of the curvilinear structure as a geodesic path. However, the derived geodesic paths are prone to yielding the shortcuts or short branches combination problems, especially when the target structures have strong tortuosity, long Euclidean distance, complex topologies or complicated background. The geodesic models with curvature regulations may reduce the risk of the problems. However, they are not always suitable in many practical applications due to the curvature-penalized geodesic models treat the centerline of curvilinear structures as the globally optimization. Moreover, these models equipped with static metrics only take into account the point wise geometry features. As an example is shown in Fig. 1, the target artery vessel locates near the vein vessel with stronger appearance features and intersects with it. We can get that the derived curvature-penalized geodesic path tends to evolve along the structures with strong appearance features, that is, the short branches combination problem occurs as described in Fig. 1c. According to the prior information that the tubular features vary slowly along the same target curvilinear structure, it requires the geodesic metric not only utilizes the appearance features, but also the continuity of the features. Therefore, we propose a dynamic curvature-penalized geodesic metric embedded with the appearance feature coherence penalty and local bending constraint, which enables the proposed metric to considering more useful local and nonlocal image features, simultaneously. We make a test and the result is depicted in Fig. 1d. The proposed model can avoid the above mentioned problems as much as possible.

4. Dynamic Curvature-penalized Geodesic Metric

The prior information that the appearance features vary smoothly along the same curvilinear structure is utilized in this work to track the curvilinear target from the complex tree networks. Different from the current curvature-penalized geodesic methods only considering the tubular appearance features, we also take into account the nonlocal coherence properties of these features. Furthermore, the nonlocal path feature is also exploited to steer the evolution of the geodesic path. The proposed metric based on those features involving the local bending constraint and the tubular features coherence property enables to force the geodesic path passing through the target curvilinear structure correctly.

4.1. Appearance Features with Coherence Enhancement

The appearance feature is usually capable of distinguishing the target from the tree structures and the background, but it is hard to identify the correct appearance feature belonging to the target within the crossing region, resulted from that two crossed structures have different appearance features, which is prone to shortcuts or short branches combination problems in the geodesic-based curvilinear tracking applications. To avoid this problem, an asymmetric oriented Gaussian kernel associated to the orientation information is constructed for appearance feature coherence enhancement [33], which helps to discriminate the appearance features in the overlapped regions. In this work, we introduce two ways to characterize the tubular appearance features by the orientation scores and the image gray levels for the metric construction, which are suitable for different curvilinear detection applications. We exploit the asymmetric oriented Gaussian kernel to obtain the coherence enhanced appearance features in order to design the correct appearance features of crossing points.

4.1.1. Coherence-enhanced Orientation Scores

At first, the orientation score defined in Eq. (4) is used to estimate the tubular appearance feature, which is constructed by extending the response of OOF filter to the orientation-lifted space. In order to characterize the appearance

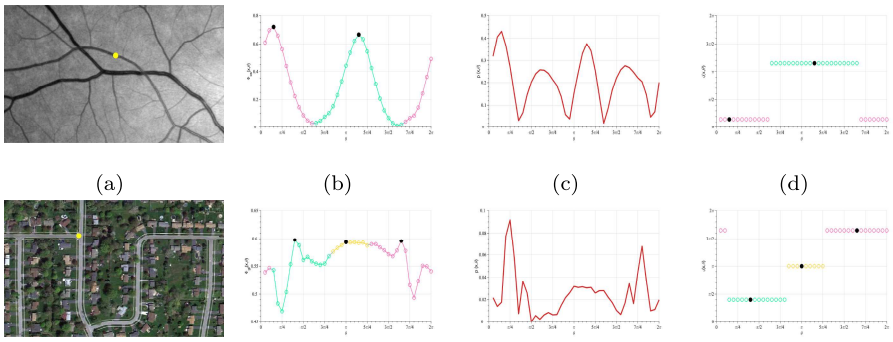

Figure 2: Examples for coherence-enhancement appearance features and orientation clustering. (**a**) and (**e**) Retinal and road images patches with points denoted as yellow dots. (**b**) The coherence-enhanced orientation score. (**f**) The multi-orientation coherence enhancing gray level score. (**c**) and (**g**) Values of the potential maps associated to the yellow points. (**d**) and (**h**) The clustered orientations.

feature correctly along the target structure, an coherence-enhanced orientation score map $\Phi_{\text{os}} : \mathbb{M} \to \mathbb{R}_0^+$ is developed in [33] and for each orientation $\theta \in \mathbb{S}^1$ it is defined as

$$\Phi_{\text{os}}(x, \theta) = \frac{\left(\mathfrak{G}_{\theta+\pi} * \left(\psi_{\text{os}}(\cdot, \theta)/\|\psi_{\text{os}}\|_\infty\right)\right)(x)}{\int_\Omega \mathfrak{G}_{\theta+\pi}(x)dx}, \tag{18}$$

where $*$ denotes the convolution operator, $\int_\Omega \mathfrak{G}_{\theta+\pi}(\mathbf{x})d\mathbf{x}$ is used for normalization, ψ_{os} is the orientation score, and $\mathfrak{G}_\theta$ is the the asymmetric oriented Gaussian kernel defined in [33] constructed by combining the oriented anisotropic Gaussian kernel [38] and a cutoff function. An example is shown in Fig. 2b, the curve indicates the coherence-enhanced orientation score of the yellow point in retina image shown in Fig. 2a.

4.1.2. Multi-orientation Coherence Enhancing Gray Level Scores

In this section, we give the method to estimate the appearance feature by image gray levels. There are two main problems existing in gray levels describing the tubular structures. One is the gray levels of the crossing section are affected by the structures with strong appearance characteristics, so it is hard to tell the correct gray levels of the target structure. The other one is the appearance

feature derived from the point-wise gray levels is susceptible to noises.

In order to overcome the above problems, we propose to exploit the gray level average value of a local square region to represent the appearance features instead of point-wise gray levels. For each point $\mathbf{x} = (x, \theta)$, a rectangular area centered at x is generated along the the direction θ. The average value of the gray levels within the local region is considered as the appearance feature for the point $\mathbf{x}$. In implementation, the local rectangular region can be approximated by the asymmetric oriented Gaussian kernel $\mathfrak{G}_\theta$, therefore the coherence enhancement can be easily implemented by filtering the image $I : \Omega \to \mathbb{R}$ over the domain Ω with the kernel $\mathfrak{G}_\theta$. The obtained multi-orientation coherence-enhanced gray level scores $\Phi_{\text{gl}} : \mathbb{M} \to \mathbb{R}_0^+$ for fixed orientation $\theta \in \mathbb{S}^1$ are formulated as

$$\Phi_{\text{gl}}(x, \theta) = \max\{0, (\mathfrak{G}_\theta * I)(x)\}. \tag{19}$$

In Fig. 2f, the curve indicates the multi-orientation coherence-enhanced gray level score of the yellow point in retina image shown in Fig. 2e. For convenience, we will collectively refer to the coherence-enhanced orientation scores Φ_{os} and the multi-orientation coherence-enhanced gray level scores Φ_{gl} as the coherence-enhanced appearance features denoted as Φ in the following parts.

4.2. Orientation Clustering

In this work, we take into account the main orientation scheme carried out by the orientation clustering to construct the metric for simplicity, that is, we only consider the appearance features along the main orientations to establish the appearance coherence measurement and exploit the main orientations to compute the local bending measurement. The main orientations can be estimated according to the locally optimal appearance features. A set of main orientations $\theta^* \in \mathbb{S}^1$ is expressed as

$$\Theta_x = \{\theta^*; \Phi(x, \theta^*) > \Phi(x, \theta), \forall \theta \in L(\theta^*, l), \text{ and } \Phi(x, \theta^*) > \mathfrak{m}(x)\}, \tag{20}$$

where Φ denotes the coherence-enhanced appearance features including coherence-enhanced orientation score map Φ_{os} (see Section 4.1.1) and the multi-orientation

coherence-enhanced gray level score map Φ_{gl} (see Section 4.1.2), $L(\theta^*, l)$ represents the interval centred at θ^* with length l, and $\mathfrak{m}$ is the mean of Φ over the orientation dimension expressed as $\mathfrak{m}(x) = (1/2\pi)\int_0^{2\pi}\Phi(x,\theta)d\theta$, which is utilized as a threshold to identify the local maxima. In Figs. 2b and 2f, the points with locally optimal appearance features are indicated by black dots.

An orientation clustering approach is given based on coherence-enhanced appearance features. For each point $\mathbf{x}_\theta = (x,\theta)$ with fixed orientation $\theta \in \mathbb{S}^1$, we try to cluster it to the corresponding point $\mathbf{x}_{\theta^*} = (x,\theta^*)$ and the clustered orientation $\theta^* \in \Theta_x$ is recognized as the main orientation to the point $\mathbf{x}_\theta$. Firstly, a potential function $\mathfrak{p} : \mathbb{M} \to \mathbb{R}_0^+$ is defined based on the coherence-enhanced appearance features Φ and its mean value $\mathfrak{m}$ along the orientation space with periodic boundary condition as

$$\mathfrak{p}(x,\theta) = |(\Phi(x,\theta) - \mathfrak{m}(x)|. \tag{21}$$

Examples of the potential values are shown in Figs. 2c and 2g. Secondly, for each point $\mathbf{x}_{\theta^*} = (x,\theta^*)$ with main orientation $\theta^* \in \Theta_x$, we compute the distance map from $\mathbf{x}_{\theta^*}$ to each point $\mathbf{x} = (x,\theta)$ along the orientation dimension based on the potential function $\mathfrak{p}$. Note that $\mathbf{x}_{\theta^*}$ and $\mathbf{x}_\theta$ have the identical physical position x. The distance value at the point $\mathbf{x}_\tau = (x,\tau)$, where $\tau \in [0, 2\pi)$, can be computed as

$$\mathcal{U}(\tau;(x,\theta_*)) = \begin{cases} \left|\int_{\theta^*}^{\tau}\mathfrak{p}(x,\theta)d\theta\right|, & \text{if } |\tau-\theta_*| \le \pi, \\ \int_0^{\theta_*}\mathfrak{p}(x,\theta)d\theta + \int_{\tau}^{2\pi}\mathfrak{p}(x,\theta)d\theta, & \text{if } \tau-\theta_* > \pi, \\ \int_0^{\tau}\mathfrak{p}(x,\theta)d\theta + \int_{\theta_*}^{2\pi}\mathfrak{p}(x,\theta)d\theta, & \text{otherwise .} \end{cases} \tag{22}$$

Finally, the orientation clustering is achieved by using the geodesic distance map $\mathcal{U}$. For each point $\mathbf{x} = (x,\theta)$, it is clustered to the main orientation point with minimum distance between them, and we can get an optimal orientation

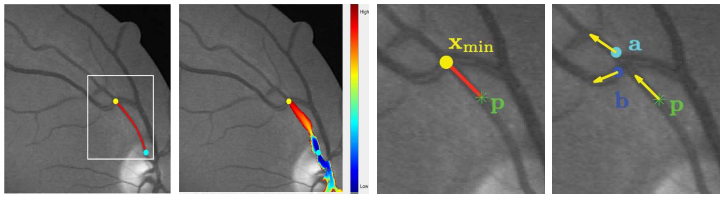

(a) (b) (c) (d)

Figure 3: (**a**) The geodesic path (red line) from the latest accepted point (yellow dot) to the source point (cyan dot). (**b**) Geodesic distances superimposed on the retinal image. (**c**) Truncated local geodesic path from the latest accepted point $\mathbf{x}_{\min}$ to the the obtained reference point $\mathbf{p}$ illustrated as green star. (**d**) The vector features denoted as yellow arrows associated to the points.

map $\varsigma : \mathbb{M} \to \Theta_x$ as

$$\varsigma(x, \theta) = \underset{\theta^* \in \Theta_x}{\arg\min}\{\mathcal{U}(\theta; (x, \theta_*))\}. \tag{23}$$

In Figs. 2b and 2f, we can observe that the points clustered to the same main orientation are denoted by the same color. The obtained optimal orientation maps are illustrated in Figs. 2d and 2h, respectively.

4.3. A New Dynamic Curvature-penalized Metric

In this part, we propose a dynamic curvature-penalized geodesic metric $\mathcal{T} : \mathbb{M} \times \mathbb{R}^3 \to \mathbb{R}_0^+$ based on the coherence penalty of appearance features and the local bending constraint. The new metric can be formulated as

$$\mathcal{T}(\mathbf{x}, \dot{\mathbf{x}}) = \mathfrak{h}(\mathbf{x})\mathfrak{g}(\mathbf{x})\mathcal{F}(\mathbf{x}, \dot{\mathbf{x}}), \tag{24}$$

where $\mathfrak{h} : \mathbb{M} \to \mathbb{R}^+$ denotes the data-driven speed function with appearance feature coherence penalty (Section 4.3.2) and $\mathfrak{g} : \mathbb{M} \to \{1, \infty\}$ presents the local bending constraint operator by utilizing the orientation lifted scheme (Section 4.3.3), which guarantee that the geodesic evolves without sharp turning. Moreover, we exploit the elastica metric $\mathcal{F}$, see Eq. (9) to encode the curvature information .

4.3.1. Reference Point Detection

In this work, we introduce the appearance feature coherence penalty and local bending constraint into the classic curvature-penalized geodesic metric. These nonlocal features are constructed by searching for an extra reference point in the orientation-lifted space. This reference point can be derived from the local truncated geodesic paths by the backtracking strategy, thanks to the single front propagation nature of the fast marching algorithm.

As described in section 3.2, the geodesic path can be tracked by solving the gradient descent ODE in Eq. (16) on the associated distance map. Here we describe the approach to search for the reference point from a local geodesic path. In the course of the fast marching front propagation, the geodesic distance map is computed within the regions where the wavefront already visited. Therefore, it is possible to extract a geodesic path from the point $\mathbf{x}$ inside the wavefront, which connects to the source point $\mathbf{s}$ by utilizing the gradient descent ODE on the obtained geodesic distance map. Given a prescribed criterion, the reference point can be identified from the truncated local geodesic path.

From the viewpoint of implementation, the geodesic path $\mathcal{C}_{\mathbf{x},\mathbf{s}} = (\mathcal{G}_{x,s}, \varrho)$ parameterized by its arc-length is easily backtracked in the orientation-lifted space, where $\varrho \in \mathbb{S}^1$ depicts the orientation information of the path and $\mathcal{G}_{x,s}(\cdot) \in \Omega$ denotes the planar curve that is obtained by projecting the orientation-lifted geodesic path into the image domain. Let $|\mathcal{G}_{x,s}|$ be the Euclidean length of the projected path $\mathcal{G}_{x,s}$. The reference point indicated as $\mathbf{p} = (p, \theta_p)$ is detected from the geodesic path $\mathcal{C}_{\mathbf{x},\mathbf{s}}$, such that the projected path of the local geodesic satisfies the prescribed criteria $|\mathcal{G}_{x,p}| = \Gamma$ and $\Gamma \in \mathbb{R}^+$ is a given constant. In Fig. 3a, we observe the geodesic path can be tracked where the geodesic distance map has been computed shown in Fig. 3b. The local truncated geodesic path from the latest accepted point $\mathbf{x}_{\min}$ with length Γ is backtracked denoted in Fig. 3c to obtain the reference point $\mathbf{p}$.

4.3.2. Appearance Feature Coherence Penalty

Once the reference point $\mathbf{p} = (p, \theta_p)$ is recognized, the non-local feature related to the appearance feature coherence measurement can be constructed based on the coherence-enhanced orientation score map in Eq. (18) or the multi-orientation coherence-enhanced gray level score map in Eq. (19). For simplicity, the appearance feature coherence penalty ϕ for the point $\mathbf{x}$ is formulated based on the optimal orientation map ς as

$$\phi(\mathbf{x}) = \exp(\mu|\Phi(x, \varsigma(\mathbf{x})) - \Phi(p, \theta_p)|) \tag{25}$$

where μ is a positive constant to control the strength of consistency penalization and $\varsigma(\mathbf{x})$ is the main orientation that the point $\mathbf{x}$ clustered to on the optimal orientation map ς. When the point $\mathbf{x}$ and its corresponding reference point $\mathbf{p}$ are located at the same curvilinear structure, the value of $\phi(\mathbf{x})$ should be low according to the slow-varying prior for the appearance features. Then we can get the image data-based cost function $\mathfrak{h} : \mathbb{M} \to \mathbb{R}^+$ embedded with the appearance feature coherence penalty as

$$\mathfrak{h}(\mathbf{x}) = \exp(-\alpha\, \psi_{\text{os}}(\mathbf{x})) \cdot \phi(\mathbf{x}) \tag{26}$$

where the weighted parameter α is a positive constant as defined in Eq. (11).

4.3.3. Local Bending Constraint Operator

Although the appearance feature coherence penalty can effectively avoid the shortcuts and short branches combination problems in many complicated situations, it is still hard to distinguish the target from neighboring structures with similar appearance features. Therefore, the local bending constraint operator $\mathfrak{g} : \mathbb{M} \to \{1, \infty\}$ is constructed by the bending measure derived from the reference point in the orientation-lifted space. Different from the bending measure estimated by two extra points from the local geodesic path in [31, 32], only one reference point is needed in this work benefiting from the orientation-lifted scheme.

In the orientation-lifted space, a vector feature is designed to indicate the tubular direction. We consider the unit vector η_θ related to the orientation

$\theta \in \mathbb{S}^1$ as the vector feature to depict the tubular direction as yellow arrows in Fig. 3(d). According to the definition, we can get two vector features from the backtracked reference point and the current point within the wavefront, which are constructed in the course of the fast marching front propagation. Note that we take into account the main orientation from the optimal orientation map ς of the current point $\mathbf{x} = (x, \theta)$ to establish the vector feature. For the reference point $\mathbf{p} = (p, \theta_p)$, the orientation can be derived from the backtracked orientation-lifted geodesic path made up of positions and orientations. Then, the local bending measure $\chi : \mathbb{M} \to [-1, 1]$ for the point $\mathbf{x}$ is estimated by the angle between two vector features associated to the reference point $\mathbf{p} = (p, \theta_p)$ as

$$\chi(\mathbf{x}) = \frac{\langle \eta_{\theta_p}, \eta_{\varsigma(\mathbf{x})} \rangle}{\|\eta_{\theta_p}\| \, \|\eta_{\varsigma(\mathbf{x})}\|}, \tag{27}$$

where $\langle \cdot, \cdot \rangle$ is the scalar product operator. We get that a small value of χ illustrates a geodesic path of strong bending.

Finally, the local bending constraint operator $\mathfrak{g} : \mathbb{M} \to \{1, \infty\}$ is defined as

$$\mathfrak{g}(\mathbf{x}) = \begin{cases} 1, & \chi(\mathbf{x}) > \chi_0, \\ +\infty, & \text{otherwise}, \end{cases} \tag{28}$$

where χ_0 is a threshold for the bending measure χ. According to the prior information that the direction of the curvilinear structure usually varies smoothly, the bending constraint operator is designed to steer the geodesic path evolution without large bending. When the value of bending measure $\chi(\mathbf{x}) > \chi_0$, the local geodesic path has small bending and $\mathfrak{g}(\mathbf{x}) = 1$, which means the fast marching front propagates as usual. Otherwise the local geodesic path may turn sharply, we set $\mathfrak{g}(\mathbf{x}) = +\infty$ to froze the point causing high bending.

Given an example in Fig. 3d, $\mathbf{p}$ represents the reference point, $\mathbf{a}$ and $\mathbf{b}$ are points located at the front. If $\mathbf{a}$ is the current *Accepted* point, we can get the angle between the two vector features derived from $\mathbf{a}$ and its reference point $\mathbf{p}$ are small, so $\mathfrak{g}(\mathbf{x}) = 1$ and the geodesic path evolves smooth. If $\mathbf{b}$ is the current *Accepted* point, the obtained angle is large which may cause high bending of the geodesic, therefore we froze the evolution by set $\mathfrak{g}(\mathbf{x}) = +\infty$. In summary,

an appropriate threshold is effective to avoid the shortcut or short branches combination problems.

Algorithm 1 Dynamic Metric-based Front Propagation

Input: The appearance feature Φ, points $\mathbf{s}$ and $\mathbf{q}$.

Output: Geodesic distance map $\mathcal{D}_{\mathbf{s}}$.

Initialization:

- Set $\mathcal{D}_{\mathbf{s}}(\mathbf{s}) \leftarrow 0$, $\mathcal{Q}(\mathbf{s}) \leftarrow Trial$.
- Set $\mathcal{D}_{\mathbf{s}}(\mathbf{x}) \leftarrow \infty$, $\mathcal{Q}(\mathbf{x}) \leftarrow Far$, $\forall \mathbf{x} \in \mathbb{M}_h \setminus \{\mathbf{s}\}$.

while stopping criterion is not reached **do**
  Set $\mathcal{Q}(\mathbf{x}_{\min}) \leftarrow Accepted$;
  Backtrack the local geodesic path from $\mathbf{x}_{\min}$;
  Find the reference point $\mathbf{p}$;
  Compute the bending measure $\chi(\mathbf{x}_{\min})$ via Eq. (27);
  if $\chi(\mathbf{x}_{\min}) \leq \chi_0$ **then**
    Set $\mathcal{D}_{\mathbf{s}}(\mathbf{x}_{\min}) \leftarrow \infty$;
  else
    for all $\mathbf{y} \in \mathcal{S}^{-1}(\mathbf{x}_{\min})$ and $\mathcal{Q}(\mathbf{y}) \neq Accepted$ **do**
      Set $\mathcal{Q}(\mathbf{y}) \leftarrow Trial$;
      Estimate appearance feature coherence penalty ϕ via Eq. (25);
      Update metric $\mathcal{T}$ via Eq. (24);
      Update distance value $\mathcal{D}_{\mathbf{s}}(\mathbf{y})$;
    end for
  end if
end while

4.4. Fast Marching Implementation

4.4.1. Fast Marching Fronts Propagation Scheme

The Hamimtonian fast marching (HFM) method [30] is an effective numerical solver to the Eikonal equations with respect to curvature-penalized models. We refer to [30] for the details on the analysis of the discretization of the cor-

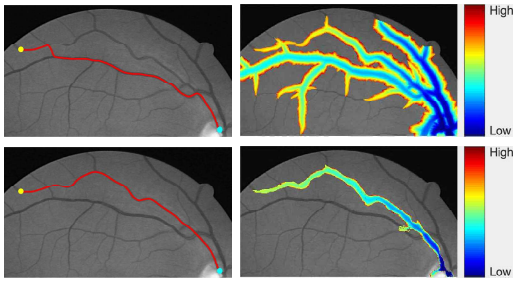

Figure 4: **Row 1:** The geodesic path derived from the FE model [28] (left) and the geodesic map superimposed on the retinal image (right). **Row 2:** The geodesic path computed by the proposed model (left) and the geodesic map superimposed on the retinal image (right).

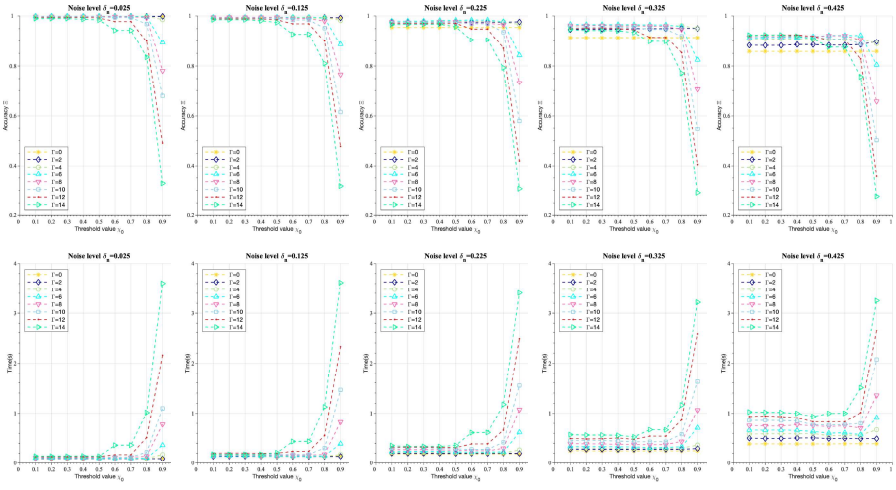

Figure 5: The sensitivity of the tracking result corresponding to the backtracked truncated geodesic length Γ and local bending threshold χ_0. **Row 1:** The detection accuracy. **Row 2:** The running times.

responding Eikonal equations. As discussed in [30], the HFM is performed in the discretization domain $\mathbb{M}_h := \mathbb{M} \cap (h\mathbb{Z}^2 \times (h\mathbb{Z} \backslash 2\pi\mathbb{Z}))$, where h is the discretization scale. During the fast marching front evolves, the geodesic distance is computed, meanwhile a label map $\mathcal{Q} : \mathbb{M}_h \to \{Far, Trial, Accepted\}$ is also estimated. In initialization, we set $\mathcal{Q}(\mathbf{x}) = Far$ for all the grid points $\mathbf{x} \in \mathbb{M}_h \backslash \{\mathbf{s}\}$ with geodesic distance $\mathcal{D}_{\mathbf{s}}(\mathbf{x}) = \infty$ associated to the source point $\mathbf{s}$, and $\mathcal{Q}(\mathbf{s}) = Trial$ with $\mathcal{D}_{\mathbf{s}}(\mathbf{s}) = 0$.

The definition of the neighbourhood system is crucial in the fast marching method. We denote by $\mathcal{S}(\mathbf{x})$ the metric-dependent neighbourhood of a grid point $\mathbf{x} \in \mathbb{M}_h$. Its inverse neighbourhood is defined as $\mathcal{S}^{-1}(\mathbf{x}) := \{\mathbf{y} \in \mathbb{M}_h; \mathbf{x} \in \mathcal{S}(\mathbf{y})\}$, which means the point $\mathbf{y}$ belongs to the neighbourhood of point $\mathbf{x}$. In the geodesic distance update iteration, a point $\mathbf{x}_{\min} \in \mathbb{M}_h$ with minimum geodesic distance value among all the $Trial$ points is tagged as *Accepted*. Once the latest *Accepted* point is obtained, the geodesic distance for each point $\mathbf{y} \in \mathcal{S}^{-1}(\mathbf{x})$ with $\mathcal{Q}(\mathbf{s}) \neq Accepted$ can be updated.

4.4.2. Dynamic Metric-based Fronts Propagation Implementation

In this section, we give the method to update the curvature-penalized metric $\mathcal{T}$ dynamically during the fast marching fronts evolve, which can be achieved by combining the fronts propagation scheme and the locally truncated geodesic backtrack strategy.

During the geodesic distance computing process, the latest *Accepted* point $\mathbf{x}_{\min}$ is detected from the $Trial$ points. We can backtrack a geodesic path $\mathcal{C}_{\mathbf{x}_{\min},\mathbf{p}} = (\mathcal{G}_{x_{\min},p}, \cdot)$ from the point $\mathbf{x}_{\min}$, where $\mathbf{p}$ is the detected reference point corresponding to $\mathbf{x}_{\min}$. The reference point $\mathbf{p}$ is derived from the backtracked geodesic path when the Euclidean curve length of the truncated geodesic satisfying the criteria $|\mathcal{G}_{x_{\min},p}| = \Gamma$. In the following, the reference point is used for all neighbouring points of $\mathbf{x}_{\min}$ labeled as $Trial$. Then the bending constraint operator and appearance feature coherence penalty can be computed to update the metric $\mathcal{T}$. The bending constraint operator $\mathfrak{g}$ determines if the propagation should be halted, which is carried out by the bending constraint measure χ. If $\chi > \chi_0$, the appearance feature coherence penalty is estimated to update the metric and the fronts propagate as usual, or the front propagation is frozen, and the point is tagged as *Accepted*. The front propagation scheme is terminated till the end point has been tagged as *Accepted* or $Trial$, or all the grid points have been tagged as *Accepted* or $Trial$. More details can be found in the pseudo-code in Algorithm 1. From Fig. 4, we get that the local bending constraint carried out by the front frozen scheme is capable of forcing

the geodesic pass through the desired structure.

4.5. Discussion

The proposed method establishes the metric in a dynamic way by invoking the appearance feature coherence penalty and local bending constraint in the orientation-lifted space. The Euler-Mumford elastica model [28], the Reeds-Sheeps model [29] and the Dubins car model [30] are three state-of-the-art curvature-penalized geodesic path approaches with strong penalizations of curvature, which are all implemented by lifting the path into the configuration space of positions and orientations. The geodesic distance can be computed by the fast marching method. In this work, we give the method to construct the dynamic curvature-penalized model based on the the Euler-Mumford elastica metric. Obviously, it is easy to construct the dynamic model depending on the Reeds-Sheeps or the Dubins car models by utilizing the proposed scheme.

Finally, we analyze the run time complexity for the fast marching implementation of the proposed model. The numerical scheme in our work is established upon the HFM method associated to the metric in Eq. (9), whose complexity is $\mathcal{O}(KN \ln N)$, where N represents the number of grid points in discretized domain $\mathbb{M}_h$ and where K is the discretization parameter for the elastica metric [30]. Thus, in our model the run time complexity can be $\mathcal{O}(KN \ln N + NW)$, where W is set as the computation time for the metric update operation as introduced in Section 4.3.

5. Experimental Results

In this work, we conduct experiments on tracking tubular structures from synthetic images, vessels from retinal fundus images and roads from satellite images quantitatively and qualitatively. For the quantitatively evaluation, an accuracy measurement Ξ is defined to compare the results from the tested models with the ground truth, defined as

$$\Xi = \frac{|\mathcal{P} \cap \mathfrak{P}|}{|\mathcal{P}|}, \tag{29}$$

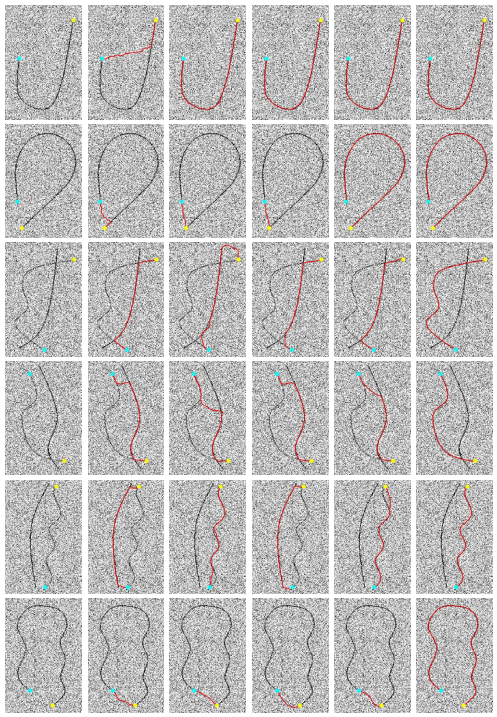

Figure 6: Qualitative comparison between different models on synthetic images. The cyan and yellow dots indicate the source and end points, respectively. The red lines represent the obtained paths from each models.

where $\mathcal{P}$ denotes the grid point set of the path tracked by the proposed model, $\mathfrak{P}$ denotes the set of grid points from the ground truth region and it is a binary segmentation if the target structures. $|\mathcal{P}|$ stands for the number of elements $\mathcal{P}$, and $|\mathcal{P} \cap \mathfrak{P}|$ represents the number of grid points of $\mathcal{P}$ passing through the ground truth region $\mathfrak{P}$. The value of the accuracy measurement Ξ ranges from 0 to 1. The higher of the accuracy measurement value indicates that the detection results are more identical to the ground truth, which means the performance of the tested models is better.

5.1. Parameter Setting

In the OOF filter, we set the standard deviation σ of the Gaussian kernel G_σ as 1.5 to construct the Hessian matrix. The possible radii ranges from $\mathcal{R}_{\min} = 1$ to $\mathcal{R}_{\max} = 8$ to generate the radius space. The weight parameter μ in Eq. (25) determines the impact from the appearance features, and α in Eq. (26) controls the influence of the appearance feature coherence penalization in the data-driven function. When the appearance feature is blurred, the α should be small and the value of μ should be high [33]. The parameter β in the metric is set as 20 to control the importance of curvature.

In the proposed model, the parameter Γ with respect to Euclidean length of the backtracked truncated geodesic path and the threshold value χ_0 for the local bending measurement are crucial in the dynamic metric construction. The sensitivity of the tracking results from the proposed model in regard to the parameters Γ and χ_0 are studied on the synthetic images. To efficiently evaluate the performance, we generated synthetic images with six types of curvilinear structures containing ones have high curvature, long Euclidean distance or crossing with each other as shown in column 1 of Fig. 6. Each structure has three different radii $r \in \{1, 2, 3\}$ pixels, respectively. Besides, each kind of image has three scales with size of 150×100, 225×159 and 300×200 grid points. All images are normalized and added Gaussian noises with 21 levels from $\sigma_n = 0$ to $\sigma_n = 0.5$. Each level of noise is added 10 times independently. Finally, a number of 11340 synthetic images are used for the experiments. We get that as the level of noises increases, the advantage of the local bending constraint becomes obvious. An appropriate combination of the parameters Γ and χ_0 used in the proposed dynamic metric can helpfully avoid the shortcuts and short combination problems to tracking the target structures correctly. Some experimental results with different noised levels are shown in Fig. 5. Both the accuracy and running time values depicted in Fig. 5 are the average of results from all images with same noise level. We consider $\Gamma = 6$ and $\chi_0 = 0.8$ as reasonable choice for the metric. It turns out that longer paths require more computation time and too high bending threshold lead to miss some target structures. All the

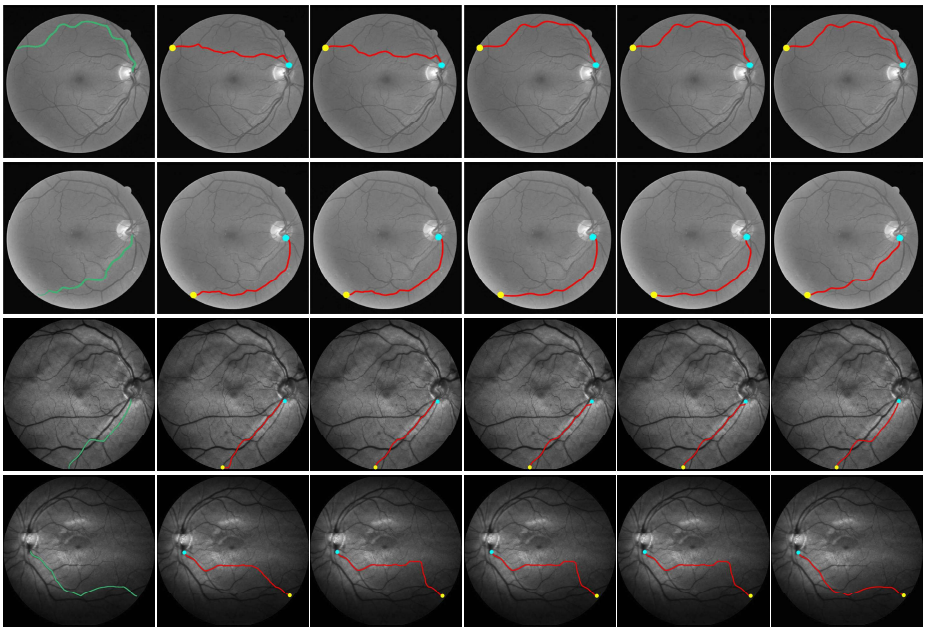

Ground truth Aniso dIso FSR FE Proposed

Figure 7: Qualitative comparison of different models on retinal images of DRIVE dataset (**Rows 1-2**) and IOSTAR dataset (**Rows 3-4**). The green line depicts the ground truth of the target structure. The cyan and yellow dots indicate the source and end points, respectively. The red lines represent the obtained minimal paths from each model.

experiments are performed on a standard Intel Core i7 of 3.2 GHz architecture with 64Gb RAM.

5.2. Qualitative Comparison with State-of-the-art Metrics

We also compared the proposed dynamic curvature-penalized metrics with the state-of-the-art geodesic models, including the progressive geodesic model with progressive isotropic dynamic metric (dIso) [31], the geodesic model with anisotropic Riemannian metric (Aniso) [23], the Euler-Mumford elastica model (FE) [28] and the Reeds-Sheeps models (FSR) [29]. The dIso model [31] introduced the local bending constraint to the isotropic metric [10] with aiming to overcome the shortcuts problems existing in the traditional isotropic geodesic method. The Aniso metric [23] exploits the anisotropic tubular features to han-

Origin Aniso dIso FSR FE Proposed

Figure 8: Qualitative comparison results of different models on satellite images. The cyan and yellow dots indicate the source and end points, respectively. The red lines represent the obtained minimal paths from each model.

dle the problems. Both the FE and FSR models take into account the curvature penalization to get the smooth geodesic paths. In this work, the proposed dynamic curvature-penalized metric is built based on the FE metric and regarded as Proposed metric. For the experiment on synthetic images and retinal images, the coherence-enhanced orientation score in Eq. (18) is used to compute the appearance feature coherence penalization. We exploit the multi-orientation coherence-enhanced gray level score in Eq. (19) to construct the appearance feature coherence penalization in the road detection from the satellite images.

Firstly, we compare the Proposed metric with the Aniso metric, the dIos metric, the FSR metric and the FE metic on the synthetic images. The structures are described in 5.1 detailedly. The goal is to detect the target structure between the prescribed points in column 1 of Fig. 6. In columns 2-6, we show part of the results (red line) on the synthetic images with size of 300×200 and

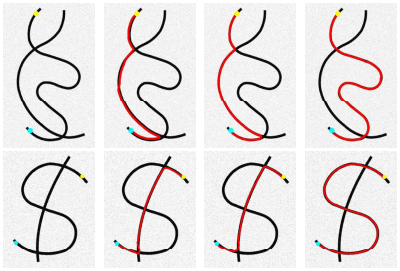

Figure 9: Comparative results on synthetic images containing structures with same gray levels. The cyan and yellow dots indicate the source and end points, respectively. The red lines represent the obtained minimal paths from each model.

Gaussian noise $\sigma_n = 0.5$. The radius of the structure is one pixel. The proposed minimal path prefers to pass through the curvilinear structures locally smooth. The geodesic path associated to the Proposed metric has the ability to delineate the desired structures correctly, especially for the structures with long euclidean distance and crossing structures. In the synthetic image and the following retinal image experiment, the parameters are set as $\alpha = 5$ and $\mu = 10$ in the image data-driven cost function.

In Fig. 7, we compare the performances of the Aniso metric, the dIos metric, the FSR metric, the FE metic and the Proposed metric on the retinal images from the DRIVE [39] and IOSTAR datasets [40]. The ground truth of the target structure is shown as green line in column 1. The comparative results are illustrated in columns 2 to 6. We also observe the shortcuts or the short branches combination problem occurs on the images in columns 2 to 5, where the obtained paths combining the segments with strong appearance features. Although, different improvements have been made in the state-of-the-art metrics to solve problems. Especially the FSR and FE metrics considering the curvature penalization are capable of solving the problems in some extent. However, it is difficult for both the metric to get the accurate results in the situation of extracting a weak target structure with strong tortuosity especially when the target is close to another structure with strong appearance features. The

geodesic path derived from the Proposed metric depicts the target structures correctly in column 6, which benefits from the appearance feature coherence penalization scheme and the front freezing strategy.

In Fig. 8, we illustrate the minimal paths derived from the state-of-the-art metrics and the proposed metric on the satellite images with aiming to tracking the roads [5]. The expected curvilinear structures have long distance and high tortuosity between ource point and end point as shown in column 1. The classic metrics fail to detect the target depicted in columns 2 to 5, while the Proposed metric can detect the desired structures accurately shown in column 6. In this experiment, the multi-orientation coherence-enhanced gray level score is used to compute the appearance feature coherence penalization. We set $\alpha = 3$ and $\mu = 20$ for the road detection in the image data-driven cost function.

In Fig. 9, we illustrate the gosesic paths derived from the FSR metric, FE metric and the Proposed metric in the case that the gray levels of the target structures are almost identical to its neighboring ones. The Proposed metric is based on the coherence-enhanced gray level score and the parameters are same as those in the above road detection experiment. In column 1, the two structures are crossed with each other. The target is the one with long euclidean distance and high tortuosity between two prescribed points. The minimal path models with the FSR metric and FE metric both fail to detect the expected structures as shown in columns 2 and 3. The Proposed metric is able to detect the structure accurately shown in column 4. Besides, a minimal path model associated with a dynamic Riemannian metric embedded with an appearance feature coherence penalty is recently proposed in [33] to extract tubular structures from the complicated vessel tree networks. However, it is difficult to track the crossed structures with same gray levels. Our Proposed metric benefiting from the front freezing scheme has the ability to solve this problem and follow the target structure.

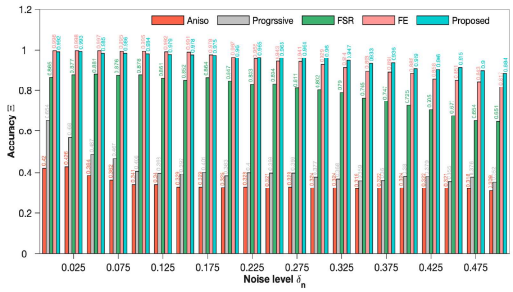

Figure 10: Average values of Ξ for evaluating the performance of the considered models in synthetic images.

Table 3: Average values of Ξ for evaluating the performance of the considered models in artery vessels tracing on retinal images from the DRIVE and IOSTAR datasets

Datasets	Aniso	dIso	FSR	FE	Proposed
DRIVE	59.99%	61.14%	58.51%	62.71%	**94.18**%
IOSTAR	80.21%	87.60%	89.38%	85.63%	**96.27**%

5.3. Quantitative Comparison

In this part, we quantitatively compare the performance of the Aniso metric, the dIos metric, the FSR metric, the FE metic and the Proposed metric on synthetic and retinal images. The accuracy measurement Ξ is utilized for the evaluation the results from the tested models with the ground truth.

The information corresponding to the synthetic images are described detailedly in 5.1. Each level of Gaussian noises with 21 levels from $\sigma_n = 0$ to $\sigma_n = 0.5$ is added 10 times independently for each scale image containing. The average values of the accuracy measurement Ξ derived from different metrics in each noise level is illustrated in Fig. 10. We can get that the curvature-penalized geodesic models including the FSR metric, the FE metic and the Proposed metric achieve better performance than the Aniso metric and the dIos metric. As the noise level increases, the model with Proposed metric shows significant advantages and get robust results.

We also compare the proposed metric with the state-of-the-art metrics quan-

titatively on retinal images from the DRIVE [39] and IOSTAR datasets [40]. In previous works, the tubular structure detection performances are usually tested on the retinal image patches including structures crossing or close to each other. Our experiments in this work are to detect the artery structures between two prescribed points on the entire images instead of the image patches. We choose the retinal artery which is close to or crosses a vein with stronger appearance features as the target vessel structure. We take into account 107 artery vessels from the DRIVE dataset and 135 artery vessels from the IOSTAR dataset. For each target structure, the prescribed points are same for all the models. The average accuracy scores for different models are demonstrated in Table. 3. We get that the average values of Ξ derived from our proposed models in each dataset are 94.18% and 96.27%, which shows that the proposed metric has significant advantages. According to all the experiments, the results prove that the proposed models outperform the compared state-of-the-art models in both robustness and accuracy.

Limitation. The experiments above have illustrated promising results. Currently, the proposed model can only be applied to address the problem of 2-dimensional curvilinear structure extraction in an interactive manner. In future, we will extend this work to automatic curvilinear tree structure extraction and to 3D tubular structure extraction.

6. Conclusion

In this paper, we propose a new minimal path model associated with dynamic curvature-penalized metric for curvilinear structure tracking. A crucial contribution is to introduce the coherence property of appearance features and nonlocal feature into the curvature-penalized metric, by designing the appearance feature coherence penalization and local bending constraint. The metric updating scheme can exploit the prior information of tubular feature changing smoothly, which effectively reduces the risk of shortcuts and short branches combination problems to obtain more accurate and robust tracking results.

Acknowledgment

The authors would like to acknowledge the Editors and the reviewers for their valuable time to read this manuscript. This work is in part supported by the National Natural Science Foundation of China (NOs. 62102210, 61902224), the Natural Science Foundation of Shandong Province (NO. ZR2021QF029), the Shanghai Sailing Program (NO. 20YF1401500), the Fundamental Research Funds for the Central Universities (NO. 2232020D-35), the French government under management of Agence Nationale de la Recherche as part of the "Investissements d'avenir" program, reference ANR-19-P3IA-0001 (PRAIRIE 3IA Institute) and by the Taishan Scholar Foundation of Shandong Province (NO. tsqn201909137).

References

[1] J. De, et al., A graph-theoretical approach for tracing filamentary structures in neuronal and retinal images, TMI 35 (1) (2015) 257–272.

[2] X. Xu, et al., Vessel boundary delineation on fundus images using graph-based approach, TMI 30 (6) (2011) 1184–1191.

[3] Y. Wang, et al., Novel 4-D open-curve active contour and curve completion approach for automated tree structure extraction, in: Proc. CVPR, 2011, pp. 1105–1112.

[4] V. Mohan, et al., Tubular surface segmentation for extracting anatomical structures from medical imagery, TMI 29 (12) (2010) 1945–1958.

[5] E. Türetken, et al., Reconstructing curvilinear networks using path classifiers and integer programming, TPAMI 38 (12) (2016) 2515–2530.

[6] J. M. Wolterink, et al., Coronary artery centerline extraction in cardiac ct angiography using a cnn-based orientation classifier, MIA 51 (2019) 46–60.

[7] E. Cheng, Y. Pang, Y. Zhu, J. Yu, H. Ling, Curvilinear structure tracking by low rank tensor approximation with model propagation, in: Proc. CVPR, 2014, pp. 3057–3064.

[8] D. Zou, X. Chen, G. Cao, X. Wang, Unsupervised video matting via sparse and low-rank representation, TPAMI 42 (6) (2019) 1501–1514.

[9] D. Chen, et al., Vessel tree extraction using radius-lifted keypoints searching scheme and anisotropic fast marching method, JACT 10 (4) (2016) 224–234.

[10] H. Li, et al., Vessels as 4-D curves: Global minimal 4-D paths to extract 3-D tubular surfaces and centerlines, TMI 26 (9) (2007) 1213–1223.

[11] E. J. Bekkers, et al., Nilpotent approximations of sub-Riemannian distances for fast perceptual grouping of blood vessels in 2D and 3D, JMIV 60 (6) (2018) 882–899.

[12] S. Kho, P. Lee, W. Lee, M. Ki, H. Byun, Exploiting shape cues for weakly supervised semantic segmentation, PR (2022) 108953.

[13] Y. Lin, J. Wu, G. Xiao, J. Guo, G. Chen, J. Ma, Bsca-net: Bit slicing context attention network for polyp segmentation, PR (2022) 108917.

[14] J. Yang, Y. Shi, Z. Qi, Learning deep feature correspondence for unsupervised anomaly detection and segmentation, PR (2022) 108874.

[15] L. D. Cohen, et al., Global minimum for active contour models: A minimal path approach, IJCV 24 (1) (1997) 57–78.

[16] Y. Rouchdy, et al., Geodesic voting for the automatic extraction of tree structures. Methods and applications, CVIU 117 (10) (2013) 1453–1467.

[17] G. Yang, et al., Vessel structure extraction using constrained minimal path propagation, AIM 105 (2020) 101846.

[18] S. Moriconi, et al., Vtrails: Inferring vessels with geodesic connectivity trees, in: Proc. IPMI, 2017, pp. 672–684.

[19] S. o. Bougleux, Anisotropic geodesics for perceptual grouping and domain meshing, in: Proc. ECCV, 2008, pp. 129–142.

[20] S. Jbabdi, et al., Accurate anisotropic fast marching for diffusion-based geodesic tractography, IJBI 2008 (2008) 2.

[21] S. Moccia, et al., Blood vessel segmentation algorithmsReview of methods, datasets and evaluation metrics, CMPB 158 (2018) 71–91.

[22] D. Lesage, et al., A review of 3D vessel lumen segmentation techniques: Models, features and extraction schemes, MIA 13 (6) (2009) 819–845.

[23] F. Benmansour, et al., Tubular structure segmentation based on minimal path method and anisotropic enhancement, IJCV 92 (2) (2011) 192–210.

[24] R. Kimmel, et al., Optimal algorithm for shape from shading and path planning, JMIV 14 (3) (2001) 237–244.

[25] M. Péchaud, et al., Extraction of tubular structures over an orientation domain, in: Proc. CVPR, 2009, pp. 336–342.

[26] E. J. Bekkers, et al., A PDE approach to data-driven sub-Riemannian geodesics in SE(2), SIAM 8 (4) (2015) 2740–2770.

[27] A. Mashtakov, et al., Tracking of lines in spherical images via sub-Riemannian geodesics in SO(3), JMIV 58 (2) (2017) 239–264.

[28] D. Chen, et al., Global minimum for a Finsler elastica minimal path approach, IJCV 122 (3) (2017) 458–483.

[29] R. Duits, et al., Optimal paths for variants of the 2D and 3D Reeds–Shepp car with applications in image analysis, JMIV 60 (6) (2018) 816–848.

[30] J.-M. Mirebeau, Fast-marching methods for curvature penalized shortest paths, JMIV 60 (6) (2018) 784–815.

[31] W. Liao, et al., Progressive minimal path method for segmentation of 2D and 3D line structures, TPAMI 40 (3) (2018) 696–709.

[32] L. Liu, et al., Anisotropic tubular minimal path model with fast marching front freezing scheme, PR 104 (2020) 107349.

[33] D. Chen, et al., Minimal paths for tubular structure segmentation with coherence penalty and adaptive anisotropy, TIP 28 (3) (2019) 1271–1284.

[34] M. Krueger, P. Delmas, G. Gimelfarb, Robust and efficient object segmentation using pseudo-elastica, PATTERN RECOGN LETT 34 (8) (2013) 833–845.

[35] J. Stuhmer, P. Schroder, D. Cremers, Tree shape priors with connectivity constraints using convex relaxation on general graphs, in: Proc.ICCV, 2013, pp. 2336–2343.

[36] W. Liao, Progressive minimal path method with embedded cnn, in: Proc.CVPR, 2022, pp. 4514–4522.

[37] M. W. Law, Three dimensional curvilinear structure detection using optimally oriented flux, in: Proc. ECCV, 2008, pp. 368–382.

[38] J.-M. Geusebroek, et al., Fast anisotropic gauss filtering, TIP 12 (8) (2003) 938–943.

[39] J. Staal, et al., Ridge-based vessel segmentation in color images of the retina, TMI 23 (4) (2004) 501–509.

[40] J. Zhang, et al., Robust retinal vessel segmentation via locally adaptive derivative frames in orientation scores, TMI 35 (12) (2016) 2631–2644.